J. Mol. Biol. (1996) **264**, 907–918

JMB

Surface Topographies at Subnanometer-resolution Reveal Asymmetry and Sidedness of Aquaporin-1

Thomas Walz[1], Peter Tittmann[2], Karl H. Fuchs[2], Daniel J. Müller[1,3] Barbara L. Smith[4], Peter Agre[4], Heinz Gross[2] and Andreas Engel[1]*

[1]*Maurice E. Müller-Institute Biozentrum, University of Basel, CH-4056 Basel Switzerland*

[2]*Institute for Cell Biology Swiss Federal Institute of Technology, CH-8093 Zürich Switzerland*

[3]*Forschungszentrum Jülich IBI-2, Structural Biology D-52425 Jülich, Germany*

[4]*Depts of Biological Chemistry and Medicine Johns Hopkins University School of Medicine, Baltimore MD 21205-2185, USA*

**Corresponding author*

Aquaporin-1 (AQP1) is an abundant protein in human erythrocyte membranes which functions as a specific and constitutively active water conducting pore. Solubilized and isolated as tetramer, it forms well-ordered two-dimensional (2D) crystals when reconstituted in the presence of lipids. Several high resolution projection maps of AQP1 have been determined, but information on its three-dimensional (3D) mass distribution is sparse. Here, we present surface reliefs at 0.9 nm resolution that were calculated from freeze-dried unidirectionally metal-shadowed AQP1 crystals as well as surface topographs recorded with the atomic force microscope of native crystals in buffer solution. Our results confirm the 3D map of negatively stained AQP1 crystals, which exhibited tetramers with four major protrusions on one side and a large central cavity on the other side of the membrane. Digestion of AQP1 crystals with carboxypeptidase Y, which cleaves off a 5 kDa intracellular C-terminal fragment, led to a reduction of the major protrusions, suggesting that the central cavity of the tetramer faces the outside of the cell. To interpret the results, sequence based structure predictions served as a guide.

Keywords: aquaporin-1; electron microscopy; atomic force microscopy; surface topography; surface identification

Introduction

Plasma membranes from tissues of diverse animal and plant species are highly permeable to water molecules, a feature mediated by the aquaporins (for reviews see Chrispeels & Agre (1994) and Knepper (1994)). This subfamily of the major intrinsic protein (MIP) family comprises integral membrane proteins that function as constitutively active water-selective pores. The archetypal member of the aquaporins, the 28 kDa channel-forming integral protein (CHIP), has been discovered in red blood cells (Denker *et al*., 1988; Smith & Agre, 1991), and is now designated as AQP1. Radiation inactivation studies of erythrocyte membranes indicated that the water pore has a size of 30 kDa (van Hoek *et al*., 1991). Identification of the AQP1 gene (Preston & Agre, 1991) allowed its expression in *Xenopus laevis* oocytes (Preston *et al*., 1992) to demonstrate the water pore activity. In addition, $HgCl_2$ which inhibits the osmotic water permeability of erythrocyte membranes (Macey & Farmer, 1970) also abolished the water flow through oocyte membranes induced by the expression of AQP1 (Preston *et al*., 1993).

The water permeability has been determined by reconstitution of highly purified AQP1 protein into proteoliposomes (Zeidel *et al*., 1992, 1994), and into two-dimensional (2D) lipid-protein crystals (Walz *et al*., 1994b). In both cases, stopped-flow measurements yielded an osmotic water permeability of $\sim 3 \times 10^9$ water molecules per AQP1 monomer per second, the same value found for native water pores in erythrocyte membranes. Osmotic water permeability measurements at different temperatures revealed an Arrhenius activation energy of 2 to 3 kcal/mol (Preston *et al*., 1992; Walz *et al*., 1994b), which is similar to that for the diffusion of water in bulk solution. Since AQP1 is highly selective for water and does not allow passage of ions or other small solutes such as urea (Zeidel *et al*., 1994), a narrow and highly specific water pore

Abbreviations used: 2D, two-dimensional; 3D, three-dimensional; CHIP, channel-forming integral protein; MIP, major intrinsic protein; AQP1, aquaporin-1; TEM, transmission electron microscope; SSNR, spectral signal-to-noise ratio; AFM, atomic force microscope.

0022–2836/96/500907–12 $25.00/0

structure is expected with a cysteine residue (C189) which may be reversibly blocked with mercuric ions (Preston *et al*., 1993).

Hydrodynamic (Smith & Agre, 1991) and electron microscopical studies (Walz *et al*., 1994a) showed that solubilized AQP1 forms tetramers. Tetramers bound to a wheatgerm agglutinin column with a ratio of approximately three unglycosylated to one glycosylated protein, indicating that there is at least one glycosylated AQP1 per tetramer (Smith & Agre, 1991). Tetramers have also been found by freeze–fracture studies of AQP1 proteoliposomes (Verbavatz *et al*., 1993). However, site-directed mutagenesis (Preston *et al*., 1993), and radiation inactivation studies (van Hoek *et al*., 1991) suggested that the functional unit of AQP1 is the monomer. Therefore, the tetramer, which is found under all conditions examined so far, contains four independent water-conducting pores. This resembles the situation of bacterial porins, which form stable trimers with three independent pores (Cowan, 1993).

Structural analyses of AQP1 became possible due to the propensity of this protein to form well-ordered 2D crystals upon reconstitution of solubilized tetramers in the presence of phospholipids (Mitra *et al*., 1994; Walz *et al*., 1994a,b). Projection maps of negatively stained samples showed tetramers arranged in a square array with lattice vectors $a = b = 9.6$ nm and eight AQP1 monomers per unit cell (Mitra *et al*., 1994; Walz *et al*., 1994b). Higher resolution projection maps were obtained by electron crystallography of either glucose-embedded (Jap & Li, 1995; Walz *et al*., 1995) or vitrified AQP1 2D crystals (Mitra *et al*., 1995). All three projection maps revealed a trapezoid-shaped AQP1 subunit; however, they differ substantially in the central region of the monomer. The projection maps derived from glucose-embedded crystals exhibited a clearly resolved mass density in the center of the trapezoid-shaped subunit (Jap & Li, 1995; Walz *et al*., 1995). In contrast, there is a density minimum at this location in the map computed from vitrified 2D crystals (Mitra *et al*., 1995). In all three maps, several density maxima are distinct which can be interpreted as projections of α-helices along their axes. This suggests that AQP1 is composed mainly of transmembrane α-helices and contradicts a porin-type β-barrel fold proposed by Fischbarg *et al*. (1995).

In spite of the wealth of 2D data on the AQP1 structure, information on its 3D mass distribution is sparse. A three-dimensional reconstruction from tilted projections of negatively stained 2D crystals unveiled an unexpected asymmetry of the tetramer with respect to the membrane plane (Walz *et al*., 1994a). In the study presented here this asymmetry of AQP1 is further characterized by the analysis of biologically active 2D crystals with electron and atomic force microscopes. Moreover, the cytosolic side of AQP1 is identified by digestion of the 2D crystals with carboxypeptidase Y which cleaves off a C-terminal fragment of about 5 kDa.

Results

In Figure 1 the correlation averages of negatively stained and freeze-dried rotary-shadowed 2D

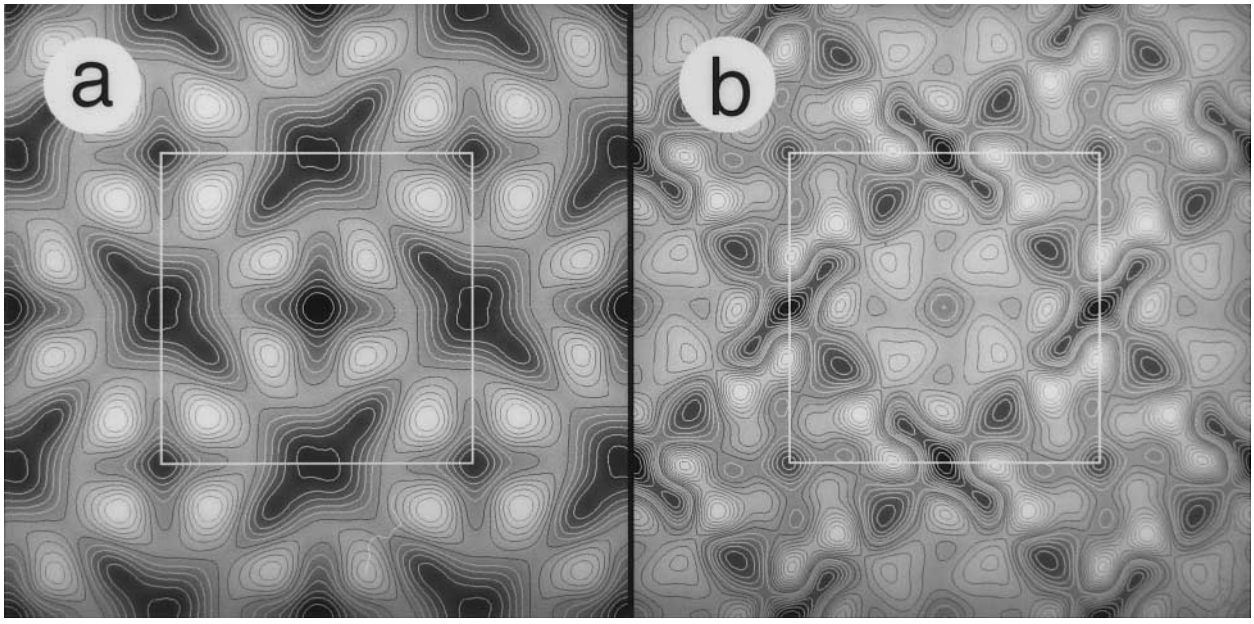

Figure 1. 4-fold symmetrized correlation averages from AQP1 2D crystals. The unit cell, which has a side length of 9.6 nm and houses two tetramers, is outlined in white. (a) In the average calculated from negatively stained 2D crystals, the projection structure of the two adjacent tetramers, which are incorporated into the membrane in opposite orientations look very similar, except that they are mirror images of each other. The average in (b) shows the sum of six correlation averages calculated from freeze-dried specimens rotationally shadowed with Ta/W at 45° elevation to reveal surface information. Therefore, the two tetramers in the unit cell display different structures.

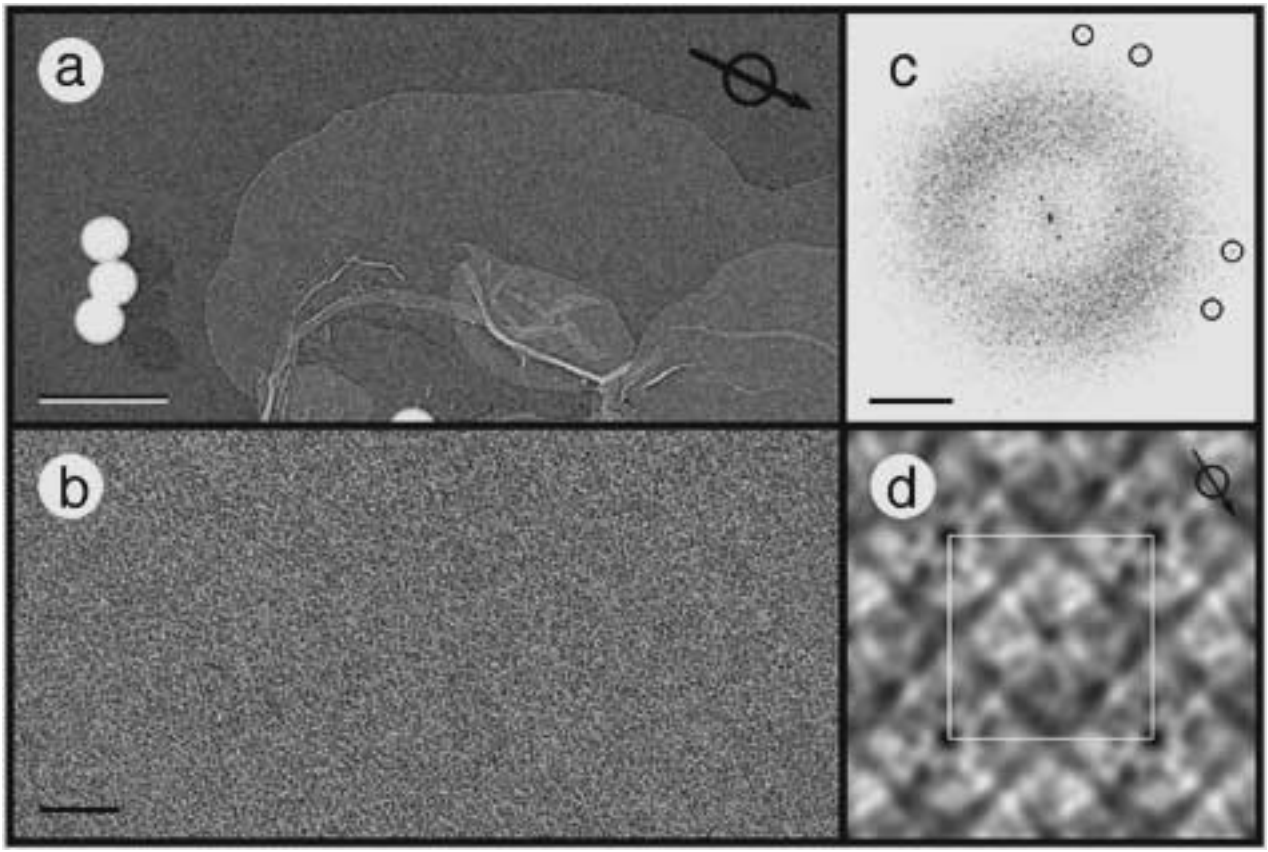

Figure 2. Electron microscopy and image processing of a unidirectionally metal-shadowed AQP1 2D crystal. (a) The low magnification overview shows a large, vesicular 2D crystal after freeze drying and unidirectional metal shadowing. The shadowing direction is estimated from the shadow cast of the coprepared latex spheres. (b) The high magnification view (×96,000) of the same vesicle does not exhibit any periodic features. (c) The power spectrum of the same area, however, shows very sharp diffraction spots. Diffraction orders 7($\pm$5) and 5($\pm$7) at a resolution of 1.1 nm are marked. (d) In the unsymmetrized correlation average, the two tetramers in the unit cell (outlined in white) display a clearly different structure. As result of the unidirectional shadowing, the 4-fold symmetry of the AQP1 tetramer is lost. Scale bars represent 0.5 μm in (a), 25 nm in (b), and 2.5 nm^{-1} in (c). The side length of (c) corresponds to 19.2 nm. The arrows in (a) and (d) indicate the shadowing direction.

AQP1 crystals are compared. Both reveal the tetrameric organization of AQP1, but whereas all tetramers are rather similar after negative staining (Figure 1a), two types are distinguished after rotary shadowing (Figure 1b). This confirms that the tetramers are incorporated into the membrane in opposite orientations (Walz *et al*., 1994a). One unit cell of 9.6 nm side length (white squares in Figure 1) thus houses two tetramers, one being right-side-out and the other one being inside-out.

A rich morphology is revealed by rotary shadowing with tantalum/tungsten (Ta/W; 45° elevation angle). The tetramer in the center of the unit cell appears quite homogeneous and is resolved into eight domains. Four domains at the corners of the tetramer are circular, while four larger triangular domains are located in-between. The four adjacent tetramers reveal a windmill-like right-handed structure, which is formed by four trilobed, elongated, domains lining the edges of the tetramer. Shape and orientation of the depressions in the center of the two oppositely incorporated tetramers resemble those of the cross-shaped stain accumulations about the 4-fold axes in the map of negatively stained specimens (Figure 1a). However, the central depression of the tetramer in the center of the outlined unit cell is less pronounced than those of the adjacent four tetramers. With a side length of about 6 nm, the tetramers appear larger than in the projection map of the negatively stained specimens. In addition, the tetramers are not rotated about the 4-fold axes with respect to each other. Accordingly, the diamond-shaped stain accumulations between the tetramers seen in negatively stained samples are represented by narrow, cross-shaped indentations in the correlation average from rotationally shadowed specimens (Figure 1b).

A low magnification overview of a freeze-dried vesicular AQP1 2D crystal unidirectionally shadowed with Ta/W is shown in Figure 2a. Micrographs of shadowed deglycosylated AQP1 2D crystals taken at ×96,000 with a CCD camera (pixel size 24 μm) displayed no periodic structure at all (Figure 2b), indicating that the surface corrugation is small. However, calculated power spectra revealed very sharp diffraction spots up to the reciprocal lattice order 7,6 indicating a resolution of

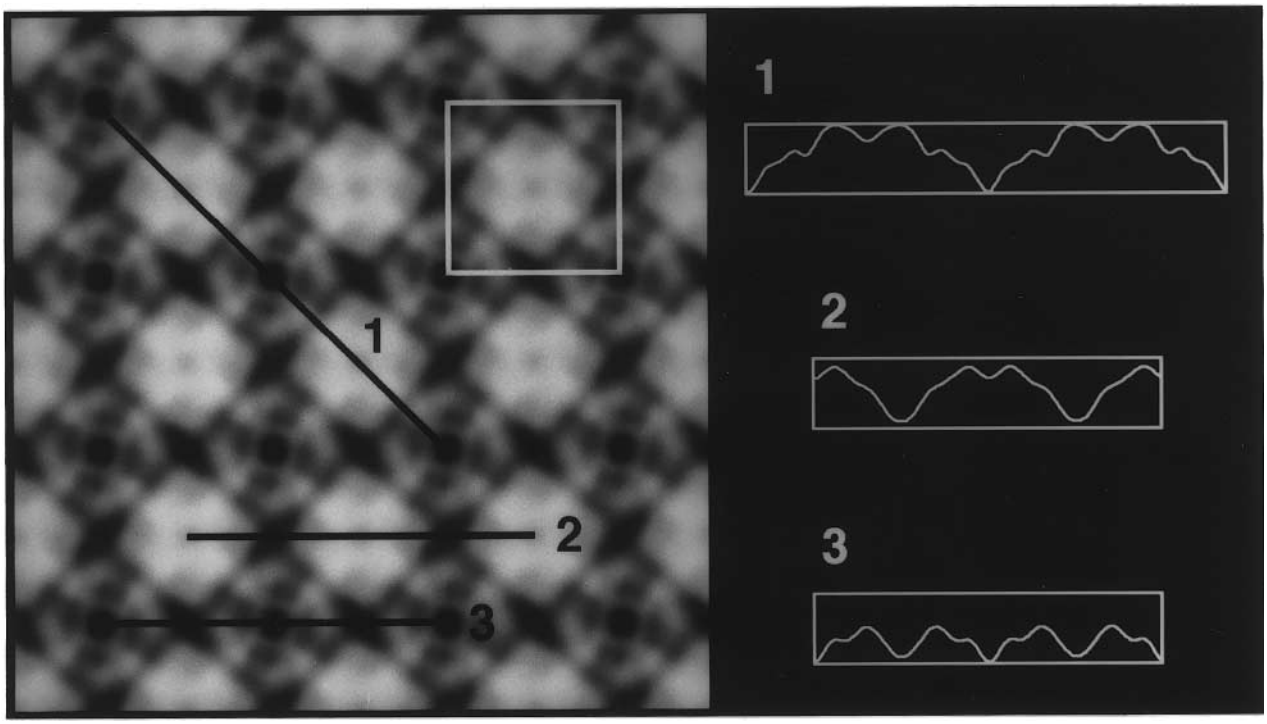

Figure 3. Surface reconstruction from a unidirectionally shadowed AQP1 2D crystal. The top view of the reconstruction is displayed in gray levels that are proportional to the height. The view demonstrates that the central tetramer in the unit cell outlined in white protrudes much more from the membrane than the adjacent tetramers. The height profiles along the marked lines 1, 2, and 3 reveal the height of the lipid surface, the major protrusion, and the central cavity. The side length of the surface reconstruction corresponds to 38.4 nm.

1.04 nm (see Figure 2c; diffraction spots 5($\pm$7) and 7($\pm$5) which correspond to a resolution of 1.12 nm) are marked. After correlation averaging over 700 motifs from the area which yielded the diffraction pattern displayed in Figure 2c, the tetramers can clearly be seen (Figure 2d). As a result of unidirectional shadowing the 4-fold symmetry is lost. Nevertheless, the windmill-like features of one AQP1 surface is evident and even the finest resolved features, with distances of 0.8 to 1.5 nm, show the directional nature of the shadowing process. Therefore, decoration effects (non-uniform distribution of metal grains due to preferential nucleation) and also the influence of the contrast of the specimen itself can be neglected. According to the radial correlation function (Saxton & Baumeister, 1982) and the spectral signal-to-noise ratio (SSNR) criterion (Unser *et al*., 1987) a resolution of 0.9 nm was achieved.

Surface reliefs of AQP1 crystals were reconstructed from single micrographs exploiting the 4-fold symmetry (Smith & Kistler, 1977; Guckenberger, 1985). The difference in the vertical positions of two adjacent tetramer surfaces was revealed by a reconstruction technique, which involves a frequency-dependent treatment of the signal-to-noise ratio during the reconstruction (Fuchs *et al*., 1995). In Figure 3 the top view of a relief is presented with gray levels that are proportional to the height of the structure. Again, the square-shaped tetramers can be seen clearly. Neighboring tetramers are only slightly rotated with respect to each other, but exhibit a pronounced difference in brightness. This reflects a substantial difference in the protein mass protruding from the two sides of the lipid bilayer, as further documented by the height profiles along the marked lines 1, 2, and 3. On one side, the four protrusions surround a small depression about the 4-fold axis. On the other side, a complex depression with a windmill-shaped disposition of small peripheral protrusions and a central cavity about the 4-fold axis is seen. In addition, the gaps separating neighboring tetramers display the characteristic cross-shape observed with rotationally shadowed specimens. The surface data are remarkably reproducible. Reconstructions from four different crystals with different shadowing azimuth (angle between lattice lines and shadowing direction) showed almost identical height profiles (data not shown).

Surface topographs of native AQP1 2D arrays were also recorded in buffer solution with the atomic force microscope (AFM). Low magnification recordings (Figure 4a) reveal the flatness of the adsorbed AQP1 2D crystalline sheets. From lattice defects such as circled in Figure 4a, the height of monolayered sheets was determined to 5.8($\pm$0.3) nm (n = 66). In addition, lattice fragments embedded in the bilayer allowed the height difference between protein and lipid membrane to be measured, 1.3($\pm$0.2) nm (n = 6). At higher

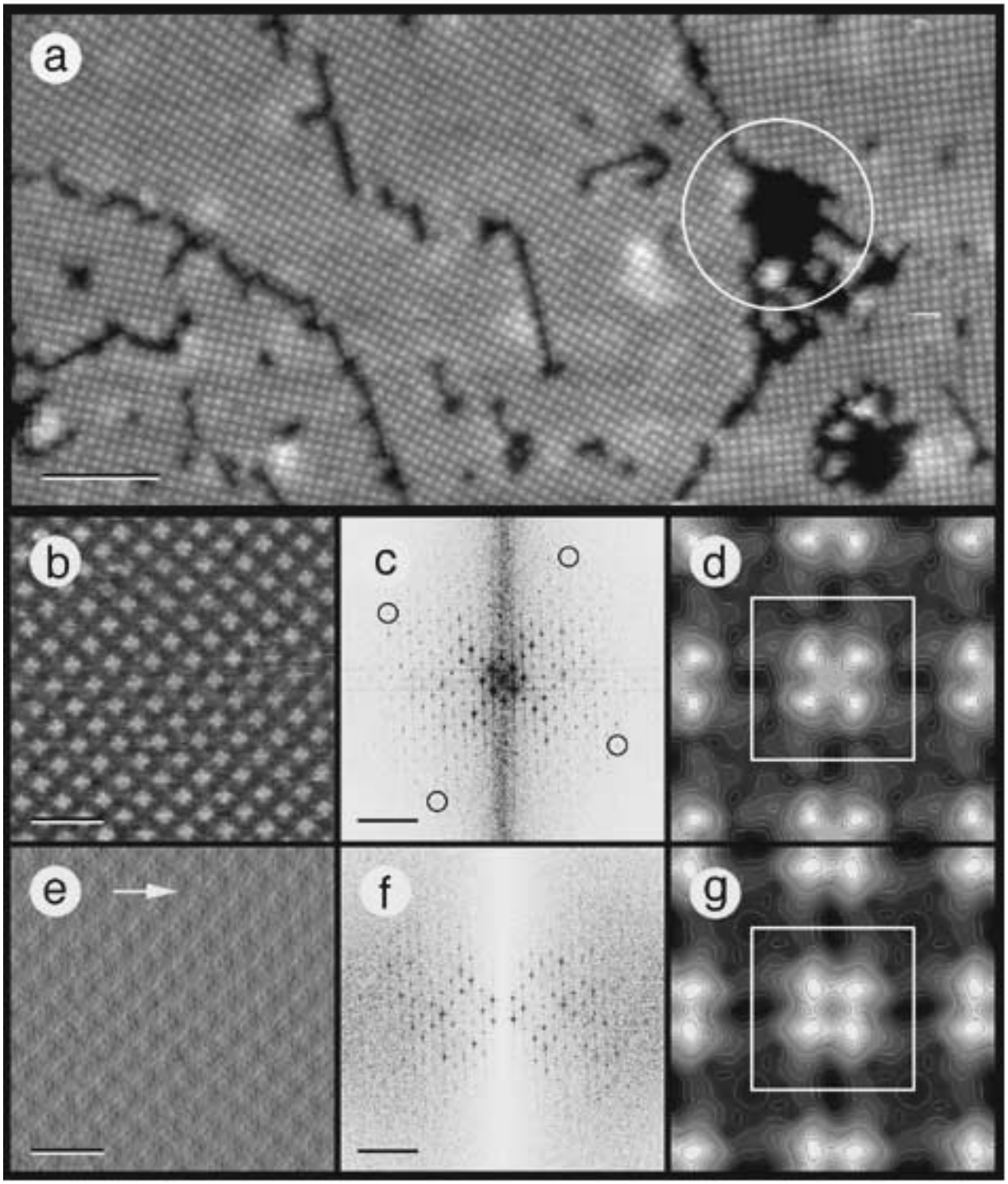

Figure 4. Atomic force microscopy image of a native AQP1 2D crystal. (a) The overview was recorded in buffer solution (150 mM KCl, 20 mM Tris-HCl (pH 8.2)) at a loading force of about 0.2 nN, scan frequency 4.7 lines/second (512 pixel). The AQP1 crystal is fragmented, exhibiting cracks and holes where the thickness of the layer is determined. (b) At high magnification, the height signal displays the major tetrameric protrusions of 1.1 nm height. (c) In the diffraction pattern calculated from the area shown in (a), diffraction spots up to the reciprocal lattice order 9,2 can be discerned, corresponding to a resolution of 1.04 nm. (d) The correlation average reveals mainly one tetramer per unit cell, while the other tetramer is represented by a pronounced depression with windmill-shaped peripheral protrusions of 0.5 nm height. (e) The error signal simultaneously acquired with the height signal displayed in (b) has the characteristics of a crystal surface metal shadowed along the fast scan direction (arrow). (f) Accordingly, the corresponding diffraction pattern exhibits a gap perpendicular to the fast scan direction. (g) The surface relief reconstructed from the error signal using the algorithm developed for the analysis of freeze-dried metal shadowed samples exhibits similar features as the height signal. Scale bars represent 100 nm in (a); 20 nm in (b) and (e); and 2.5 nm^{-1} in (c) and (f). The side length of (d) and (g) corresponds to 19.2 nm.

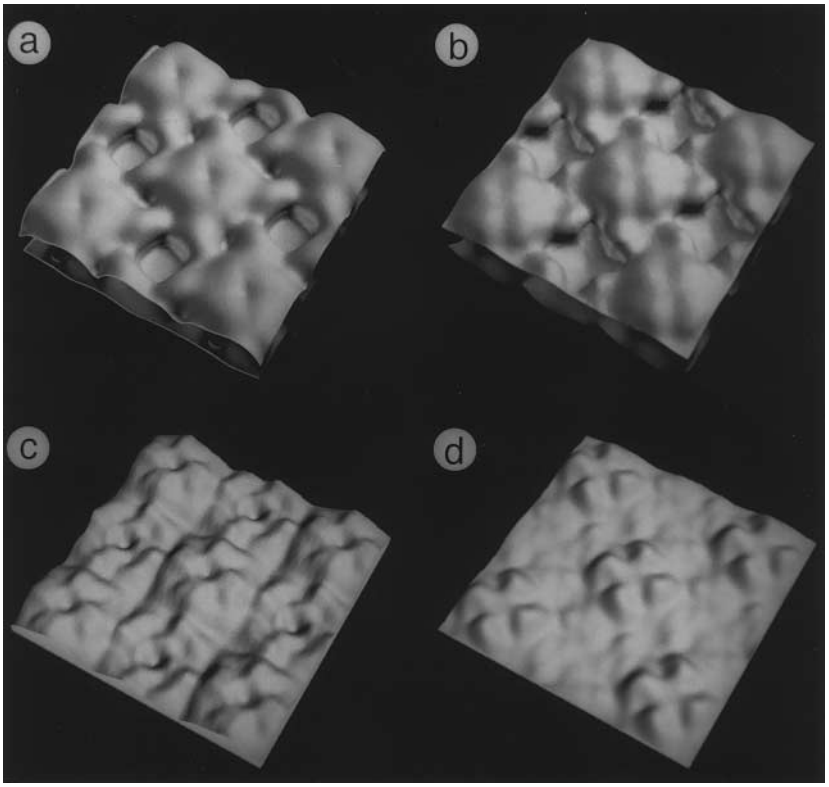

Figure 5. Perspective views of the AQP1 2D crystal surface. (a) Surface facing the carbon film calculated from the 3D map of negatively stained crystals. (b) Surface facing the vacuum. (c) Relief reconstructed from correlation averages of unidirectionally shadowed specimens. (d) Surface topograph recorded with the atomic force microscope. All surfaces possess a side length of 20.6 nm and are displayed in the same orientation. As a result of the $p42_12$ symmetry of the crystal, cytosolic and extracellular surfaces of the tetramer are shown. The pronounced asymmetry of the AQP1 tetramer with respect to the membrane plane can be seen in all four perspective views.

magnification (Figure 4b), individual unit cells exhibiting quadruple protrusions can clearly be seen in the unprocessed image. The diffraction pattern (Figure 4c) displays a homogenous resolution of the recorded image along the fast scanning direction and perpendicular to it. Diffraction spots of the reciprocal lattice order 9,2 visible in the calculated power spectrum indicate a resolution of 1.04 nm. To further assess the lateral resolution, the radial correlation function as well as the SSNR profile were calculated from 134 unit cells to yield 0.9 nm and 1.1 nm, respectively. Finally, the reproducibility of the height values were estimated from the highest values in the standard deviation map to 0.2 nm (Schabert & Engel, 1994). This corresponds to 18% of the corrugation amplitude, $1.1(\pm 0.2)$ nm ($n = 15$). The 4-fold symmetrized correlation average (Figure 4d) documents the distinct difference between the surfaces of the two oppositely incorporated tetramers. This average is in excellent agreement with the surface relief reconstruction (Figure 3). The tetramer in the center of the unit cell is clearly resolved into four domains surrounding a small central depression. Adjacent tetramers exhibit a less pronounced surface texture with small peripheral protrusions arranged in a windmill-shaped pattern. The four maxima of the central tetramer are at exactly the same positions as the corresponding maxima of the reconstructed surface relief shown in Figure 3. The height difference between major and minor protrusions, $0.6(\pm 0.2)$ nm ($n = 15$), allows the sections of the relief reconstruction to be scaled (Figure 3). As a result of the finite tip size, however, the central depressions of the adjacent tetramers are not as distinctly outlined as in the surface relief reconstruction. The error signal (Putman *et al*., 1992) displayed in Figure 4e exhibits the characteristic features of an unidirectionally metal-shadowed freeze-dried protein lattice. This is reflected by the diffraction pattern in Figure 4f which demonstrates the loss of information perpendicular to the fast scan direction and the attenuation of the low diffraction orders. As the error signal (Putman *et al*., 1992) and the projected density of unidirectionally metal-shadowed surfaces (Smith & Kistler, 1977) are related from a mathematical point of view, the relief reconstruction algorithm described by Fuchs *et al*. (1995) was used to determine the relief shown in Figure 4g.

Figure 5 compares the surface reliefs obtained by isocontouring a 3D reconstruction from tilt series of negatively stained AQP1 2D crystals (Figure 5a, b; (Walz *et al*., 1994a)), the surface relief calculated from images of unidirectionally shadowed specimens (Figure 5c), and the topograph of native AQP1 2D crystals recorded in buffer solution (Figure 5d). The two perspective views of negatively stained samples represent the surface in contact with the carbon film (Figure 5a), and that facing the vacuum (Figure 5b). In the latter relief the central tetramer reveals four well-resolved protruding domains, and a pronounced height difference to the oppositely oriented, neighboring tetramers. Thus, the relief of the crystal surface that is not in contact with the carbon film is in excellent agreement with the surface reconstruction calculated from unidirectionally metal-shadowed 2D

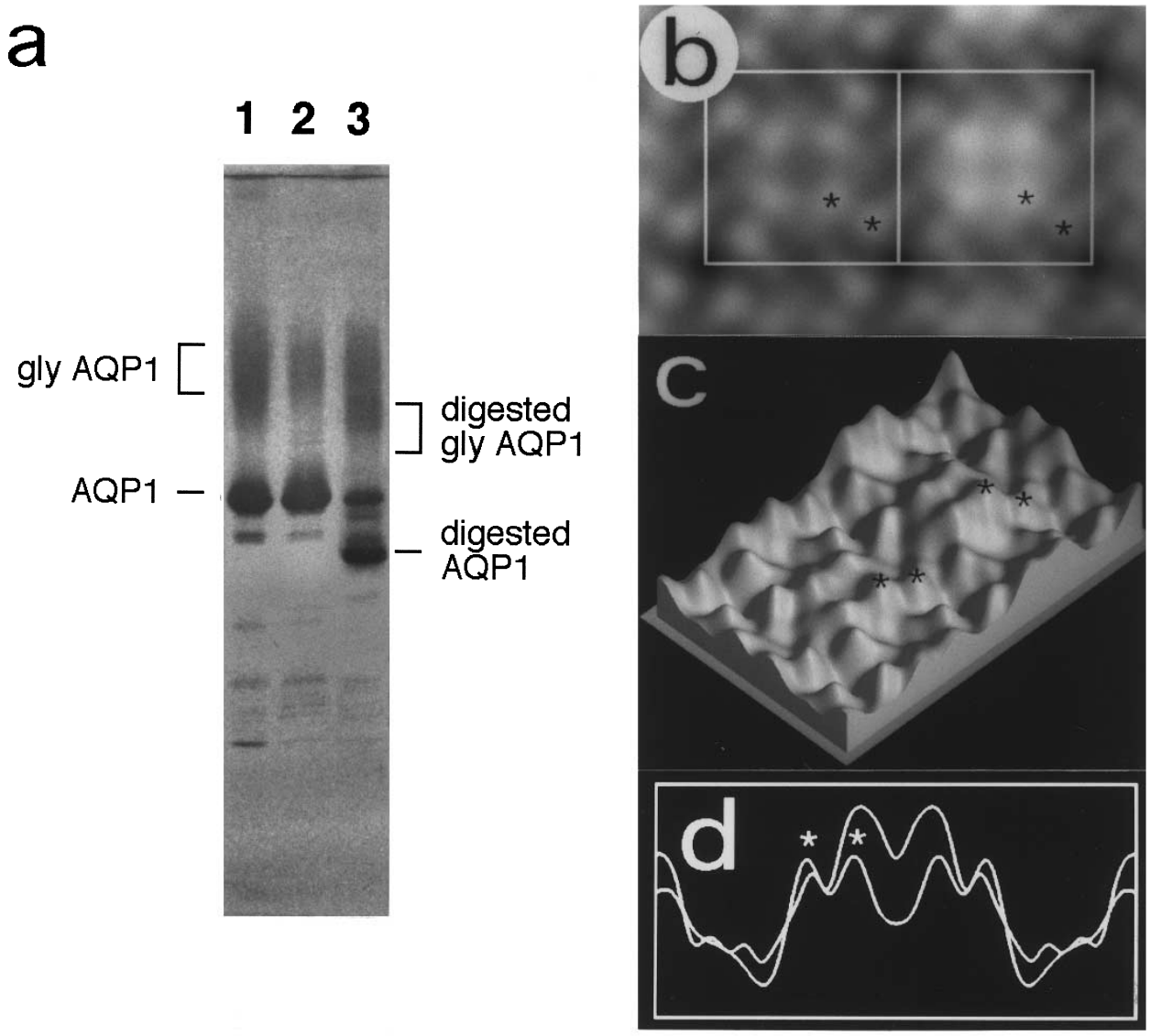

Figure 6. Carboxypeptidase Y digestion of 2D crystals to assess the sidedness of the AQP1 tetramer. (a) A silver-stained gradient gel (15 to 22.5% polyacrylamide) documenting the digestion of the reconstituted membranes: 1, untreated 2D crystals, 2, after deglycosylation with endoglycosidase F/N-Glycosidase F, and 3, after subsequent digestion with carboxypeptidase Y. (b) The surface relief reconstruction from unidirectionally metal shadowed AQP1 2D crystals which were digested with carboxypeptidase Y (left) displays a much less pronounced height difference between adjacent tetramers than observed in the surface relief from undigested samples (right). The relief on the right has been low-pass filtered to the same resolution (1.6 nm) as the relief on the left, while the minor protrusions have been used to scale the two reliefs with respect to one another. (c) Perspective view, and (d) profile approximately along the line indicated by asterisks reveal the height difference between digested and undigested AQP-1. Asterisks identify cytosolic and extracellular protrusions in (b) to (d). The unit cells of 9.6 nm side length are outlined in white.

crystals (Figure 5c). In particular, the pronounced height difference between the two sides of the tetramer is evident. This height difference is also distinct in the topograph recorded with the AFM (Figure 5d). In addition, the small domains which surround the large central cavities of the tetramers stand out more clearly in the perspective view than in the map displayed in Figure 4d.

To determine the sidedness of the AQP1 tetramer, carboxypeptidase Y was used to digest deglycosylated 2D crystals. By this treatment, a C-terminal fragment of about 5 kDa is removed from the native protein (Smith & Agre, 1991). Figure 6a shows an SDS gel of untreated (lane 1), with endoglycosidase F/N-Glycosidase F deglycosylated (lane 2), and subsequently with carboxypeptidase Y digested (lane 3) AQP1 2D crystals. From the reduction of the smeared protein band in the higher molecular weight range, it is evident that a significant fraction of the reconstituted AQP1 has been deglycosylated. The remaining smeared band in the higher molecular weight range on the SDS gel (Figure 6, lane 2) is due to inside-out tetramers which were not accessible to

the endoglycosidase. Since the C terminus is known to be intracellular, right-side-out tetramers should have been protected from cleavage by carboxypeptidase Y, thus explaining the remaining band of undigested AQP1.

Carboxypeptidase Y digested AQP1 2D crystals were prepared and recorded in the same way as undigested 2D crystals. However, a much lower fraction of the imaged areas exhibited good crystalline order compared to the undigested crystals. The best images showed diffraction spots up to the sixth reciprocal lattice order indicating a resolution of 1.6 nm (data not shown). The reconstructed surface relief from such an image is shown in Figure 6b, left unit cell. Compared to the surface relief from undigested membranes rendered at the same resolution (Figure 6b, right unit cell), the major tetrameric protrusion of the AQP1 appears to be reduced after proteolysis, and the cavity in the center of this tetrameric major protrusion to be enlarged. These differences become more evident in the perspective view (Figure 6c) of the surface relief reconstructions shown in Figure 6b, and in the profiles displayed in Figure 6d.

Discussion

In contrast to the wealth of information on the projection structure of the AQP1 protein (Jap & Li, 1995; Mitra *et al*., 1994, 1995; Walz *et al*., 1994b, 1995), information on the three-dimensional (3D) mass distribution of this specific water conducting pore is sparse. A low resolution freeze–fracture study has demonstrated that AQP1 forms oligomers with four subunits that protrude from the membrane (Verbavatz *et al*., 1993). Negatively stained 2D crystals have provided a 3D reconstruction at 1.6 nm resolution (Walz *et al*., 1994a) that is presently the only information available on the 3D structure of AQP1. Thus, the goal of the work presented here was to acquire additional information on the 3D structure of AQP1 using heavy metal-shadowing techniques and atomic force microscopy.

Structure prediction and hydropathy analysis of the AQP1 amino acid sequence (Preston & Agre, 1991) and the intracellular localization of the N and C termini (Smith & Agre, 1991) led to a model based on six transmembrane helices connected by five extramembranous loops (A to E). The prominent homology between the first and the second half of the amino acid sequence (Preston & Agre, 1991; Reizer *et al*., 1993) and the experimental evidence that these repeats have opposite orientations (Preston *et al*., 1994) indicated a 3D structure of the AQP1 protein which is symmetrical with respect to the membrane plane. This was corroborated by the double mutant A73C/C189S, because its wild-type mercurial sensitivity suggested loops B and E to be arranged in a symmetrical conformation likened to an hourglass (Jung *et al*., 1994). In contrast, the 3D map reconstructed from tilt series of uranyl formate stained 2D crystals revealed an asymmetric mass distribution ((Walz *et al*., 1994a); Figure 5a, b). On one side of the lipid bilayer the AQP1 tetramer protrudes farther from the membrane and surrounds a narrower central cavity than on the other side, which exhibits a large indentation. Thus, the first 3D map of AQP1 did not confirm the symmetric structure predicted by sequence analysis and site-directed mutagenesis. One possibility to explain this discrepancy is the phenomenon of stain redistribution upon illumination with the electron beam described by Unwin & Klug (1974). Because the stain tends to accumulate during irradiation in the center of a cavity, its volume tends to be overestimated. Since the specimen had to be imaged several times in order to record a tilt series, such beam-induced artifacts could not be ruled out. However, surface reliefs calculated from low-dose images of unidirectionally metal-shadowed 2D crystals, as well as topographs recorded with the AFM of native 2D crystals in buffer solution, demonstrate the pronounced asymmetry of the aquaporin with respect to the membrane plane. Thus, the 3D reconstruction from negatively stained AQP1 arrays appears to reflect the structural features of the water pore correctly.

As result of the $p42_12$ symmetry, both surfaces of the AQP1 2D crystals should look identical. In the surface-rendered 3D reconstruction from negatively stained 2D crystals, the two surfaces revealed the same overall morphology of the unit cell, but subtle differences between the two sides of the 3D map are distinct. In Figure 5a, the four domains of the central tetramer are not as well resolved as in Figure 5b and the height difference between oppositely incorporated tetramers is less pronounced. This is explained by deformations of the specimen surface upon adsorption to the carbon film and by subsequent flattening during dehydration (Baumeister *et al*., 1986). From the 3D map alone, it was not possible to unambiguously determine which surface of the 3D reconstruction is closer to the ''real'' structure. Comparison with the surface relief reconstructed from unidirectionally metal shadowed 2D crystals (Figure 5c) and the surface topography of native 2D crystals imaged with the AFM in buffer solution (Figure 5d) clearly favors the surface representation shown in Figure 5b.

Freeze-drying and unidirectional Ta/W shadowing of AQP1 2D crystals yielded an unusually high resolution. This is the first demonstration that structural details in this resolution range can be preserved and visualized by metal shadowing. To attain such a high resolution, efforts were necessary to improve dehydration (''preservation of the structural water'' (Gross, 1987)), metal shadowing (Gross *et al*., 1985), and to minimize changes in the metal film between coating and image acquisition. By using the MIDILAB (Gross *et al*., 1990) the shadowed specimens were transferred into the microscope under high vacuum and cryo-conditions and imaged at –175°C using low dose

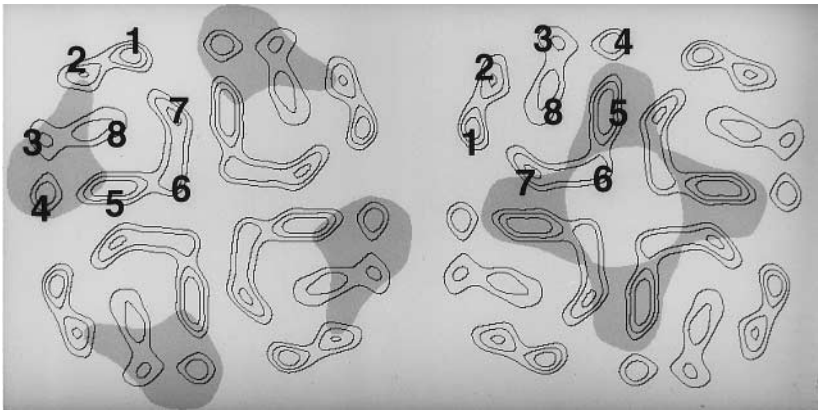

Figure 7. Projections of AQP1 tetramers from the extracellular side (left) and the cytosolic side (right). The contours represent the 6 Å projection of glucose embedded crystals (Walz *et al*., 1995). The shaded areas display the extracellular protrusions (left) and the cytosolic protrusions (right) revealed by surface relief reconstruction (Figure 3). Small extracellular protrusions may be related to loops connecting putative α-helical spans at the periphery of the tetramer (left). Density maxima 5 and 7 coincide with the cytosolic protrusion which houses the C terminus (right).

techniques. At no stage was the specimen exposed to air or warmed to ambient temperature. Under these conditions a stabilizing carbon coat, obscuring fine structural details, can be omitted. The high lateral (<1 nm) and vertical (<0.5 nm) resolution obtained suggests that the deposited metal did not migrate and recrystallize. Thus, shadowing with a small amount of Ta/W and image averaging yields a homogeneous shadow cast such as required for relief reconstruction (Fuchs *et al*., 1995). It is interesting to note that this procedure is fast and reliable. If the crystals are of high quality, results of the kind presented here can be obtained within a day. Former shadowing experiments with non-deglycosylated AQP1 2D crystals using conventional shadowing methods yielded a resolution of only 4 nm (see Walz *et al*., 1994a).

As result of its ability to observe surfaces at high resolution in buffer solution (Drake *et al*., 1989), the AFM is a powerful tool for the analysis of biomolecules. Although the image formation process is difficult to understand in depth, conditions have been found that allow topographs of protein arrays to be reproducibly acquired with the AFM at a resolution of 0.8 to 1.5 nm (Karrasch *et al*., 1994; Müller *et al*., 1995a; Schabert & Engel, 1994; Schabert *et al*., 1995). Comparison with X-ray crystallography (Schabert *et al*., 1995) and with electron microscopy (Karrasch *et al*., 1994; Müller *et al*., 1995a) demonstrated that the accuracy of the height data is in the range of a few angstroms. Hence, the AFM topographs presented here can be used to calibrate the reconstructed surface relief of shadowed crystals. Deglycosylated AQP1 crystals have a height of 5.8(±0.3) nm, as determined after calibrating the scanner with $MoTe_2$ crystals (Müller *et al*., 1995b). Steps of 1.3(±0.2) nm were observed at the edge of crystalline patches embedded in the bilayer, yielding a bilayer thickness of 4.5 nm. The peak-to-peak amplitude of high-resolution topographs is 1.1(±0.2) nm, which corresponds to the vertical drop from the central tetrameric protrusion on one side of the membrane to the bilayer surface, since the tip is too large to contour the small depression ($\emptyset \approx 1$ nm) at the center of adjacent tetramers. On the other side of the membrane, the AQP1 monomer protrudes by approximately 0.5(±0.1) nm ($n = 15$) above the bilayer. This is comparable to the signal of loops connecting helices A and B, or C and D of bacteriorhodopsin on the cytoplasmic surface (Müller *et al*., 1995a).

The error signal is the difference between the deflection of the stylus and the compensation administered by the servo system, and is governed by the properties of the AFM cantilever and the frequency response of the piezo scanner. While the tip contours the protein surface according to the tip geometry when operating within the scan speed limit (Butt *et al*., 1993), the servo system is bandwidth limited by an $1/f$ filter to prevent oscillations. Thus, the error signal corresponds approximately to the first derivative of the topography along the fast scan direction. We therefore applied the surface relief reconstruction algorithm described by Fuchs *et al*. (1995) to obtain the relief displayed in Figure 4g. The similarity between the measured relief (Figure 4d) and the reconstructed relief (Figure 4g) demonstrates the validity of this approach which will be useful when bandwidth limitations are required to prevent oscillations of the AFM servo system. However, the force induced by the cantilever deflection should be considered. For AQP1 crystals, this force amounts to 100 pN taking the force constant of the cantilever (0.1 N/m) into account. Forces of this magnitude are just sufficiently small to prevent the deformation of protein surfaces (Müller *et al*., 1995a).

As shown by Figure 6b, c, digestion with carboxypeptidase Y increases the central depression and reduces the height of the central protrusions by 0.5 nm, corresponding to a mass of approximately 3 kDa per AQP1 monomer. This identifies the major tetrameric protrusion as cytosolic, and suggests that about 40% of 5 kDa fragment cleaved off is in a disordered conformation. It is interesting to relate this observation to the dimeric AQP1 construct generated by ligation of BAM H1 restriction sites (Jung *et al*., 1994). Full

biological activity of this tandem AQP1 expressed in *Xenopus* oocytes was surprising in view of the loss of five residues between N and C termini (Jung *et al*., 1994). The possibility of C terminal disorder appears to offer an explanation of this finding which suggests that the N and C termini must be close.

Comparing the surface topography with high-resolution projection maps of AQP1 (Jap & Li, 1995; Mitra *et al*., 1995; Walz *et al*., 1995), the sidedness of the maps can be determined (Figure 7). Eight density maxima have been resolved in the maps of (Jap & Li, 1995) and (Walz *et al*., 1995), seven in the map of (Mitra *et al*., 1995). They are numbered in clockwise sequence for the tetramer projected from the cytosolic side (Figure 7, right), and in anti-clockwise sequence for the tetramer viewed from the extracellular side (Figure 7, left). The strongest of all peaks (peak 5) coincides with the cytosolic protrusion, which partly covers peak 7 as well. Therefore, density peak 5 or 7 must be related to the C terminus. Small protrusions on the extracellular surface revealed by rotary shadowing, by surface relief reconstruction, and by AFM are likely the result of loops connecting α-helices. If, as predicted by the hour-glass model (Jung *et al*., 1994), loops B and E fold back into the membrane, these small peripheral domains could be loops A and C. However, this interpretation is guided by a model from structure prediction which has been confirmed by epitope-scanning mutants (Preston *et al*., 1994), but has been challenged elsewhere. Other models described AQP1 as a four-membrane span molecule (Skach *et al*., 1994) or as a eight-membrane span molecule (Jap & Li, 1995). To resolve this question, a high resolution 3D map is required.

Materials and Methods

Reconstitution, endoglycosidase F/N-glycosidase F, and carboxypeptidase Y treatment

AQP1 was purified from human erythrocytes (Smith & Agre, 1991) and reconstituted into 2D crystals as described (Walz *et al*., 1994b). To deglycosylate the reconstituted 2D crystals, the vesicles were washed twice with 250 mM sodium acetate (pH 6), 20 mM EDTA, 10 mM β-mercaptoethanol and treated overnight at 37°C with endoglycosidase F/N-Glycosidase F (Boehringer, Mannheim, Germany). A fraction of the deglycosylated AQP1 2D crystals was washed twice with 25 mM sodium acetate (pH 6), 0.5 mM dithiothreitol and treated overnight at 37°C with carboxypeptidase Y (Sigma, St Louis, USA). Subsequently, the digested vesicles were washed twice with the above buffer and used for electron microscopical analyses.

Negative staining

To assess the crystallinity of reconstituted AQP1 membranes, negatively stained samples were recorded with a Hitachi H-7000 transmission electron microscope (TEM) and checked with an optical diffractometer as described (Walz *et al*., 1994a).

Heavy metal shadowing

Deglycosylated AQP1 2D crystals were adsorbed to glow-discharged carbon-coated 400 mesh grids, washed with double-distilled water, blotted and immediately frozen in liquid nitrogen. Submerged in liquid nitrogen at all times, the grids were mounted in specially designed grid holders, loaded on the specimen table and transferred to the pre-cooled cold stage of the MIDILAB (Gross *et al*., 1990) using a dry nitrogen counter-flow loading device. The MIDILAB is a complete freeze-drying and shadowing unit, which is permanently mounted onto the column of a Philips CM12-TEM. Specimens can be transferred back and forth to the TEM under high vacuum and cryo-conditions. Freeze drying was carried out in the MIDILAB for 2 hours at –80°C and a pressure $p \leqslant 10^{-7}$ mbar. Depending on the experiment, the samples were subsequently either rotary or unidirectionally shadowed with Ta/W at an elevation angle of 45° using an electron beam evaporator. The metal coat thickness of 0.5 nm (50 Hz) was controlled with a Balzers QSG 301 quartz monitor and a liquid nitrogen-cooled shutter. Samples were transferred to a specially designed Gatan cryoholder, and examined in the TEM at an acceleration voltage of 100 kV at $T \leqslant -175$°C. Images were recorded with a Gatan 694 slow scan CCD camera (1024^2 pixels of 24 μm edge width) under low dose conditions (<500 e^-/nm^2) at a magnification of ×96,000, corresponding to 0.25 nm pixel width at the specimen.

Images from the CCD camera were directly used for correlation averaging (Saxton & Baumeister, 1982). The resolution limits of the images were determined according to either the Fourier ring correlation (Saxton & Baumeister, 1982), or the spectral signal-to-noise ratio (Unser *et al*., 1987). All digital image processing steps performed on the metal-shadowed specimens, including surface reconstruction and presentation, were carried out as described (Fuchs *et al*., 1995) using the MILAN software package, which was developed in the Institute for Cell Biology, Swiss Federal Institute of Technology (Fuchs, unpublished software).

Atomic force microscopy

Deglycosylated AQP1 2D crystals were deposited on freshly cleaved mica discs that had been glued onto 25 mm Teflon discs fixed to magnetic holders (Schabert & Engel, 1994). The crystals were adsorbed for 10 to 30 minutes in 300 mM NaCl, 20 mM Tris-HCl (pH 7.2). Samples were subsequently washed with buffer (150 mM KCl, 20 mM Tris-HCl (pH 8.2)) to remove membranes that were not firmly attached to the substrate. For thickness measurements, the washing buffer was 300 mM KCl, 20 mM Tris-HCl (pH 8.2). A commercial AFM (Nanoscope III, Digital Instruments, Santa Barbara, CA 93117, USA) equipped with a 120 μm scanner (*j*-scanner) and a liquid cell was used. Cantilevers with a force constant of $k = 0.1$ N/m and oxide sharpened Si_3N_4 tips were purchased from Olympus (Tokyo, Japan). Operation of the AFM was performed as described (Müller *et al*., 1995b), using molybdenum ditelluride to calibrate the scanner.

Averaged unit cells were calculated after unbending the crystals, and the resolution was assessed either by the radial correlation function (Saxton & Baumeister, 1982) or the spectral signal-to-noise ratio (Unser *et al*., 1987) as described (Schabert & Engel, 1994). For corrugations smaller than the tip radius, the AFM behaves approximately like a linear system with an $1/f$ transfer function

(Engel, 1991). Therefore, the Fourier transform of the correlation averaged unit cells were weighted with a linear ramp and bandwidth limited to the measured resolution.

Acknowledgments

This work was supported by the Swiss National Foundation for Scientific Research (grant 31-36324.92 to H.G., grant 31-42435.94 to A.E., and a post-doctoral fellowship to T.W.), the National Heart, Lung, and Blood Institute of the NIH (grants HL48268 and HL33991 to P.A.), the Department of Education of the Kanton Basel-Stadt, the Deutsche Forschungsgemeinschaft (SFB 189 fellowship to D.J.M.) and the Maurice E. Müller Foundation of Switzerland.

References

Baumeister, W., Barth, M., Hegerl, R., Guckenberger, R., Hahn, M. & Saxton, W. O. (1986). Three-dimensional structure of the regular surface layer (HPI layer) of *Deinococcus radiodurans*. *J. Mol. Biol.* **187**, 241–253.

Butt, H.-J., Siedle, P., Seifert, K., Fendler, K., Seeger, T., Bamberg, E., Weisenhorn, A. L., Goldie, K. & Engel, A. (1993). Scan speed limit in atomic force microscopy. *J. Microsc.* **169**, 75–84.

Chrispeels, M. J. & Agre, P. (1994). Aquaporins: water channels of plant and animal cells. *Trends Biochem. Sci.* **19**, 421–425.

Cowan, S. W. (1993). Bacterial porins: lessons from three high-resolution structures. *Curr. Opin. Struct. Biol.* **3**, 501–507.

Denker, B. M., Smith, B. L., Kuhajda, F. P. & Agre, P. (1988). Identification, purification, and partial characterization of a novel M_r 28,000 integral membrane protein from erythrocytes and renal tubules. *J. Biol. Chem.* **263**, 15634–15642.

Drake, B., Prater, C. B., Weisenhorn, A. L., Gould, S. A. C., Albrecht, T. R., Quate, C. F., Cannell, D. S., Hansma, H. G. & Hansma, P. K. (1989). Imaging crystals, polymers, and processes in water with the atomic force microscope. *Science,* **243**, 1586–1589.

Engel, A. (1991). Biological application of scanning probe microscopes. *Annu. Rev. Biophys. Biophys. Chem.* **20**, 79–108.

Fischbarg, J., Li, J., Cheung, M., Czegledy, F., Iserovich, P. & Kuang, K. (1995). Predictive evidence for a porin-type beta-barrel fold in CHIP28 and other members of the MIP family. A restricted-pore model common to water channels and facilitators. *J. Membr. Biol.* **143**, 177–188.

Fuchs, K. H., Tittmann, P., Krusche, K. & Gross, H. (1995). Reconstruction and representation of surface data from two-dimensional crystalline, biological macromolecules. *Bioimaging,* **3**, 12–24.

Gross, H. (1987). High resolution metal replication of freeze-dried specimens. *Cryotechniques in Biological Electron Microscopy* (Steinbrecht, R. A. & Zierold, K., eds), pp. 205–215, Springer Verlag, Berlin.

Gross, H., Müller, T., Wildhaber, I. & Winkler, H. (1985). High resolution metal replication, quantified by image processing of periodic test specimens. *Ultramicroscopy,* **16**, 287–304.

Gross, H., Krusche, K. & Tittmann, P. (1990). Recent progress in high-resolution shadowing for biological transmission electron microscopy. In *Proceedings of the XIIth International Congress for Electron Microscopy, Seattle*, pp. 510–511, San Francisco Press Inc., San Francisco, USA.

Guckenberger, R. (1985). Surface reliefs derived from heavy-metal-shadowed specimens–Fourier space techniques applied to periodic objects. *Ultramicroscopy,* **16**, 357–370.

Jap, B. K. & Li, H. (1995). Structure of the osmo-regulated H_2O-channel, AQP-CHIP, in projection at 3.5 Å resolution. *J. Mol. Biol.* **251**, 413–420.

Jung, J. S., Preston, G. M., Smith, B. L., Guggino, W. B. & Agre, P. (1994). Molecular structure of the water channel through aquaporin CHIP: the tetrameric-hourglass model. *J. Biol. Chem.* **269**, 14648–14654.

Karrasch, S., Hegerl, R., Hoh, J. H., Baumeister, W. & Engel, A. (1994). Atomic force microscopy produces faithful high-resolution images of protein surfaces in an aqueous environment. *Proc. Natl Acad. Sci. USA,* **91**, 836–838.

Knepper, M. A. (1994). The aquaporin family of molecular water channels. *Proc. Natl Acad. Sci. USA,* **91**, 6255–6258.

Macey, R. I. & Farmer, R. E. I. (1970). Inhibition of water and solute permeability in human red cells. *Biochim. Biophys. Acta,* **211**, 104–106.

Mitra, A. K., Yeager, M., Vanhoek, A. N., Wiener, M. C. & Verkman, A. S. (1994). Projection structure of the CHIP28 water channel in lipid bilayer membranes at 12-angstrom resolution. *Biochemistry,* **33**, 12735–12740.

Mitra, A. K., van Hoek, A. N., Wiener, M. C., Verkman, A. S. & Yeager, M. (1995). The CHIP28 water channel visualized in ice by electron crystallography. *Nature Struct. Biol.* **2**, 726–729.

Müller, D. J., Buldt, G. & Engel, A. (1995a). Force-induced conformational change of bacteriorhodopsin. *J. Mol. Biol.* **249**, 239–243.

Müller, D. J., Schabert, F. A., Buldt, G. & Engel, A. (1995b). Imaging purple membranes in aqueous solutions at sub-nanometer resolution by atomic force microscopy. *Biophys. J.* **68**, 1681–1686.

Preston, G. M. & Agre, P. (1991). Isolation of the cDNA for erythrocyte integral membrane protein of 28 kilodaltons: member of an ancient channel family. *Proc. Natl Acad. Sci. USA,* **88**, 11110–11114.

Preston, G. M., Carroll, T. P., Guggino, W. B. & Agre, P. (1992). Appearance of water channels in *Xenopus* Oocytes expressing red cell CHIP28 protein. *Science,* **256**, 385–387.

Preston, G. M., Jung, J. S., Guggino, W. B. & Agre, P. (1993). The mercury-sensitive residue at cysteine 189 in the CHIP28 water channel. *J. Biol. Chem.* **268**, 17–20.

Preston, G. M., Jung, J. S., Guggino, W. B. & Agre, P. (1994). Membrane topology of aquaporin CHIP: analysis of functional epitope-scanning mutants by vectorial proteolysis. *J. Biol. Chem.* **269**, 1668–1673.

Putman, C. A. J., van der Werf, K. O., de Grooth, B. G., van Hulst, N. F., Greve, J. & Hansma, P. K. (1992). A new imaging mode in the atomic force microscope based on the error signal. *SPIE* **1639**, 198–204.

Reizer, J., Reizer, A. & Saier, M. H. (1993). The MIP family of integral membrane channel proteins–sequence comparisons, evolutionary relationships, reconstructed pathway of evolution, and proposed functional differentiation of the 2 repeated halves of

the proteins. *Crit. Rev. Biochem. Molec. Biol.* **28**, 235–257.
Saxton, W. O. & Baumeister, W. (1982). The correlation averaging of a regularly arranged bacterial cell envelope protein. *J. Microsc.* **127**, 127–138.
Schabert, F. A. & Engel, A. (1994). Reproducible acquisition of *Escherichia coli* porin surface topographs by atomic force microscopy. *Biophys. J.* **67**, 2394–2403.
Schabert, F. A., Henn, C. & Engel, A. (1995). Native *Escherichia coli* OmpF porin surfaces probed by atomic force microscopy. *Science,* **268**, 92–94.
Skach, W. R., Shi, L., Calayag, M. C., Frigeri, A., Lingappa, V. & Verkman, A. S. (1994). Biogenesis and transmembrane topology of the CHIP28 water channel at the endoplasmic reticulum. *J. Cell Biol.* **125**, 803–815.
Smith, B. L. & Agre, P. (1991). Erythrocyte M_r 28,000 transmembrane protein exists as a multisubunit oligomer similar to channel proteins. *J. Biol. Chem.* **266**, 6407–6415.
Smith, P. R. & Kistler, J. (1977). Surface reliefs computed from micrographs of heavy metal-shadowed specimens. *J. Ultrastruct. Res.* **61**, 124–133.
Unser, M., Trus, B. L. & Steven, A. C. (1987). A new resolution criterion based on spectral signal-to-noise ratios. *Ultramicroscopy,* **23**, 39–52.
Unwin, P. N. T. & Klug, A. (1974). Electron microscopy of the stacked disk aggregate of tobacco mosaic virus protein. II. The influence of electron irradiation on the stain distribution. *J. Mol. Biol.* **87**, 657–670.
van Hoek, A. N., Hom, M. L., Luthjens, L. H., deJong, M. D., Dempster, J. A. & van Os, C. H. (1991). Functional unit of 30 kDa for proximal tubule water channels as revealed by radiation inactivation. *J. Biol. Chem.* **266**, 16633–16635.
Verbavatz, J.-M., Brown, D., Sabolic, I., Valenti, G., Ausiello, D. A., Van Hoek, A. N., Ma, T. & Verkman, A. S. (1993). Tetrameric assembly of CHIP28 water channels in liposomes and cell membranes: a freeze–fracture study. *J. Cell Biol.* **123**, 605–618.
Walz, T., Smith, B. L., Agre, P. & Engel, A. (1994a). The three-dimensional structure of human erythrocyte aquaporin CHIP. *EMBO J.* **13**, 2985–2993.
Walz, T., Smith, B. L., Zeidel, M. L., Engel, A. & Agre, P. (1994b). Biologically active two-dimensional crystals of aquaporin CHIP. *J. Biol. Chem.* **269**, 1583–1586.
Walz, T., Typke, D., Smith, B. L., Agre, P. & Engel, A. (1995). Projection map of aquaporin-1 determined by electron crystallography. *Nature Struct. Biol.* **2**, 730–732.
Zeidel, M. L., Ambudkar, S. V., Smith, B. L. & Agre, P. (1992). Reconstitution of functional water channels in liposomes containing purified red cell CHIP28 protein. *Biochemistry,* **31**, 7436–7440.
Zeidel, M. L., Nielsen, S., Smith, B. L., Ambudkar, S. V., Maunsbach, A. B. & Agre, P. (1994). Ultrastructure, pharmacologic inhibition, and transport-selectivity of Aquaporin CHIP in proteoliposomes. *Biochemistry,* **33**, 1606–1615.

Edited by M. F. Moody

(Received 1 July 1996; received in revised form 25 September 1996; accepted 27 September 1996)